nature materials

Supplementary information

https://doi.org/10.1038/s41563-024-02002-y

Two-dimensional crystalline platinum oxide

In the format provided by the authors and unedited

Content

Online Movie 1: In-situ SEM observation of the oxidation process.

The *In situ* SEM images captured the oxidation process of Pt(111) under NO_2 atmosphere at 1000 K and 1 mbar. The uniformly increasing contrast in the secondary-electron image indicates a change in the surface work function during NO_2 oxidation. Therefore, *in situ* scanning electron microscopy observations suggest the formation of uniform layered species on the Pt(111) surface under NO_2 atmosphere at 1000 K and 1 mbar. This video dynamically demonstrates the changes in atmospheric composition and contrast in the images over time. The stable image contrast in the H_2 atmosphere and the uniformly changing image contrast in the oxidative atmosphere can be clearly distinguished and compared. The evolution of Pt surface species abstracted from this video is discussed in detail in the main manuscript.

Online Movie 2: In-situ XPS study of the oxidation process.

The composition and evolution behavior of surface species was monitored by *in situ* XPS. Movie 2 shows the evolution of O 1s spectra gathered under 1 mbar NO_2 conditions from 300 K to 1000 K. At the beginning, the surface was covered by adsorbed NO^* and O^*. With the temperature increasing, PtO_2 was formed on the surface, and the PtO_2 increased with temperature between 500 K and 750 K. Above 750 K, PtO_2 desorbed from the surface. Finally, the new species PtO_x formed on the surface at 1000 K.

Online Movie 3: Thermal expansion of the sample holder in the AP-XPS experiment.

The thermal expansion of the sample holder in the AP-XPS measurement was shown in Movie 3. As demonstrated in this figure, even a minor alteration in the sample's positioning can significantly impact the XPS signal intensity.

Online Movie 4: In-situ SEM observation of the H_2 etching process.

This video records the etching behavior of PtO_x on the Pt (9 10 7) surface under 1 mbar H_2 at 1000 K. In the first half of the video, images show the appearance of new edges at the concave corners of etching islands, and it is observed that the etching rate is faster along these edges. Individual vacancy islands grow self-similarly in a truncated equilateral triangle shape until the entire surface is completely etched. In the second half of the video, a three-dimensional reconstruction of the etched area and time demonstrates the relative expansion rates along the edge expansion direction and the formation of new edges. This is consistent with the simulation of the polar-speed bar in the main text.

Online Movie 5: LEED with electron energy increasing.

The movie showed the LEED patterns of PtO_x on the Pt(111) surface collected at different beam energies (from 10 eV to 127 eV). At lower energies, the six spots arising from the PtO_x film were very clearly visible. At higher energies, the LEED patterns from the Pt(111) substrate became clear and distinguishable.

Online Movie 6: Simulation of the α-PtO_2 decomposition.

The movie shows the MD simulation of the stability of α-PtO_2. At the beginning, the surface was covered with full layer of PtO_2. The structure corrupted at high temperatures, which means that

it is thermodynamically unstable.

Online Movie 7: Simulation of the 30° rotated α-PtO_2 decomposition.

The movie shows the MD simulation of the stability of the 30° rotated α-PtO_2. We can see the α-PtO_2 layer float on the substrate from the side view. It is thermodynamically unstable and prone to corrugation. It cannot exist specially at relevant high temperatures.

Online Movie 8: PtO_x stability simulation.

The movie shows the MD simulation of the stability of the relaxed PtO_x (30° rotated α-PtO_2 with one Pt removed). We can see all the atoms vibrates in a very small area. It means that this structural configuration of PtO_x is thermodynamically stable.

Online Movie 9: Structure evolution from PtO_2 to PtO_x.

The video shows the structure evolution from PtO_2 to PtO_x. PtO_2 was shown in the beginning, with the simulated diffraction pattern and the experimental LEED in the inserts. As the PtO_2 layer rotated 30° relative to the substrate Pt(111), the moiré pattern appeared and the simulated diffraction pattern also changed. But this structure is unstable. In the next step, one Pt atom in the unit cell was removed. The relaxed structure of this PtO_2 with one Pt removed (PtO_x) was very stable under reaction under high temperature. And the simulated diffraction pattern of this structure is also same with the experimental LEED result.

Online Movie 10: STM simulation.

The video initially presents the alignment of STEM images with the model. Subsequently, in the first half, schematic models of surface O *p*-orbitals and their corresponding electron density are showcased, revealing a spindle-shaped structure when observed from the side. When utilizing a STM, the relative position of the scanning tip and its interaction with the isosurface along the scanning line indicate that the region of highest electron density is not directly above the surface O atom but rather there is a position gap between them. In the latter part of the video, simulated STM images are demonstrated to match well with the proposed PtO_3-Pt structure.

Online Movie 11: Simulation of position gap between STM and atom model.

This video showcases the complete structural model, and a segment featuring a Pt atomic chain structure is extracted to demonstrate both top and side views, supplemented with electron density isosurfaces. The electron density isosurfaces of the surface O *p*-orbitals exhibit a spindle-shaped pattern, with the highest point of the isosurface showing a position gap from the surface O atom in the atomic model. Line profiles of the surface O positions extracted from experimental STM image and simulated STM image reveal a consistent position gap with the model's atomic positions.

Supplementary Note 1: Phase diagram of the Pt-O species

A significant body of experimental and theoretical research was devoted to unraveling the complex formation mechanisms that lead to the emergence of thin, intricate atomic structures of Pt-oxides, as indicated in Supplementary Fig. 1. [1-7] The phase diagram includes the adsorbed oxygen, surface oxide, oxide stripe, α-PtO_2 and spoked-wheel oxide.

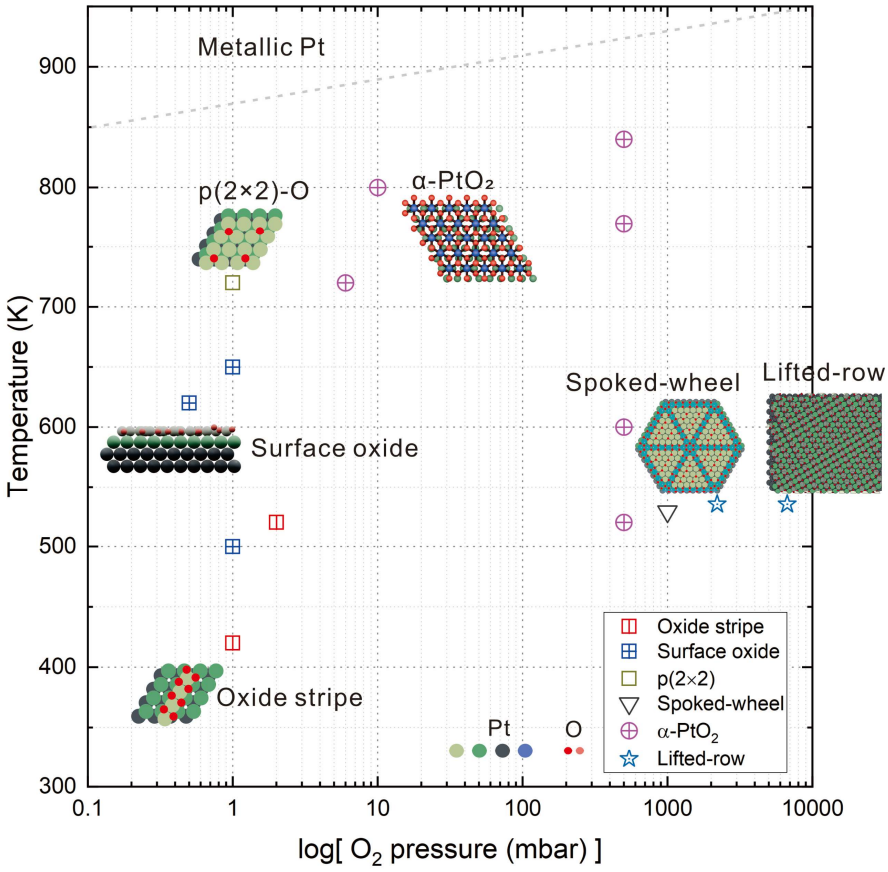

Supplementary Figure 1: Phase Diagram of Pt-O species. Phase diagram of the different Pt-O species as a function of temperature and oxygen pressure obtained from the previous studies. [1-7]

Supplementary Note 2: The cleanness of Pt(111)

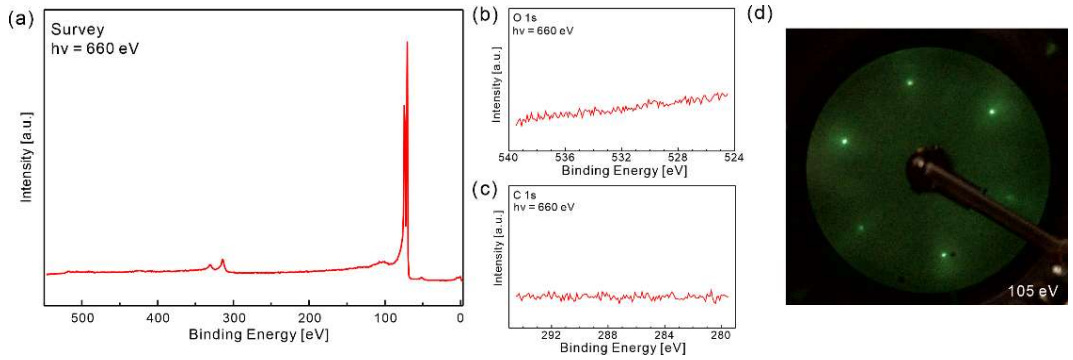

Supplementary Figure 2: XPS and LEED of the Pt(111) surface. (a) Survey, (b) O 1s, (c) C 1s, and (d) LEED pattern of Pt(111) under UHV conditions at room temperature after the cleaning procedures. The XPS spectra were collected at the photoenergy of 660 eV. The LEED pattern was taken under 105 eV.

After the same clean process (Ar^+ sputtering (1.5 keV, 10 mA, 15 min) and annealing (700 °C, 10 min)), XPS and LEED were used to show the surface's conditions. Supplementary Figure 2(a) survey, (b) O 1s and (c) C 1s spectra show that there is no oxygen and/or carbon related contaminations on the surface. The (1 × 1) LEED pattern in Supplementary Figure 2(d) indicates that the surface we studied in this work is well-ordered.

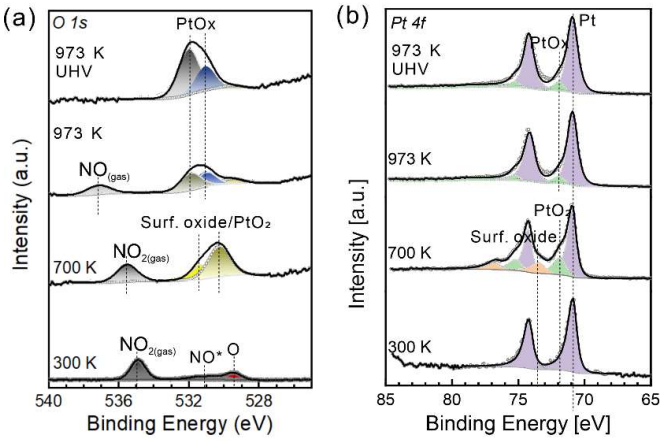

Supplementary Figure 3: XPS spectra during Pt(111) oxidation. (a) O 1s and (b) Pt 4f spectra on the Pt(111) surface under 1 mbar NO_2 from 300 K to 973 K. The spectra were collected with the photo electron kinetic energy of 120 eV.

Supplementary Note 3: The variation of the O 1s intensity on Pt(111)

This variation of the O 1s intensity under ultra-high temperatures could stem from the thermal expansion of the sample holder when subjected to ultra-high temperatures. The thermal expansion of the sample holder in the AP-XPS measurement was shown in Supplementary Figure 4. The XPS signal intensity as a function of the sample distance was shown in Supplementary Figure 5. As demonstrated in this figure, even a minor alteration in the sample's positioning can significantly impact the XPS signal intensity.

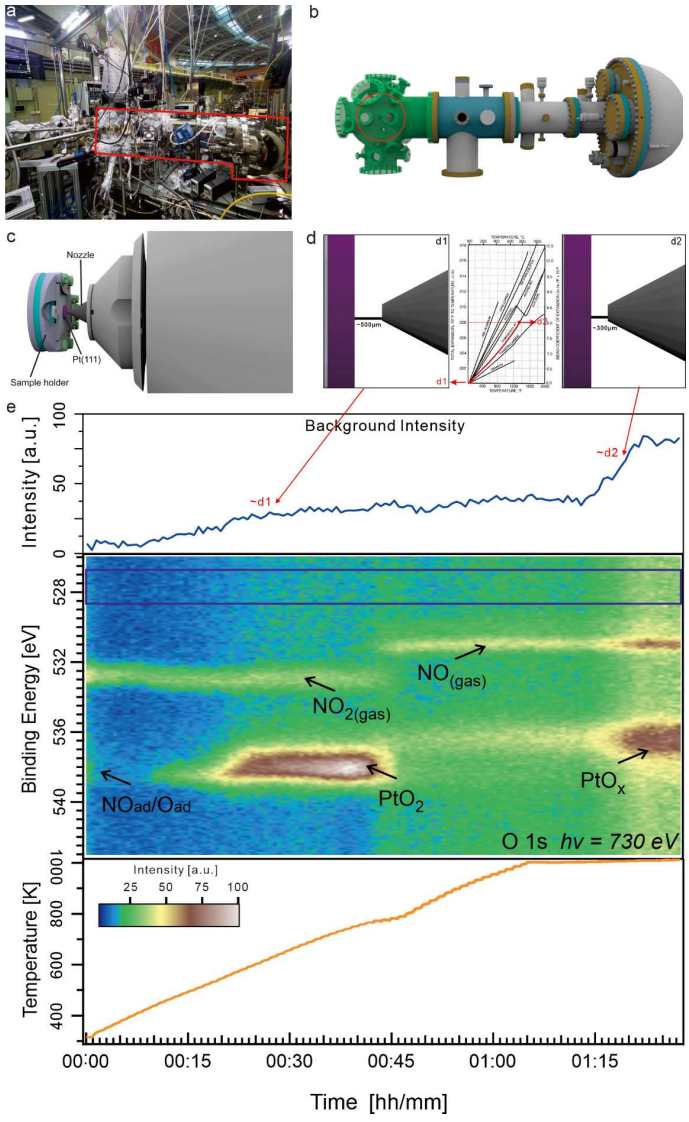

Supplementary Figure 4: The thermal expansion of the sample plate in the AP-XPS. The thermal expansion of the sample in the AP-XPS. (a) and (b) The image and model drawings of the AP-XPS setup; (c) The schematic of the sample at the AP-XPS test location; (d) The thermal expansion of the sample holder under different temperature; (e) XPS background intensity during the heating process and the O 1s spectra on Pt(111) with temperature increasing.

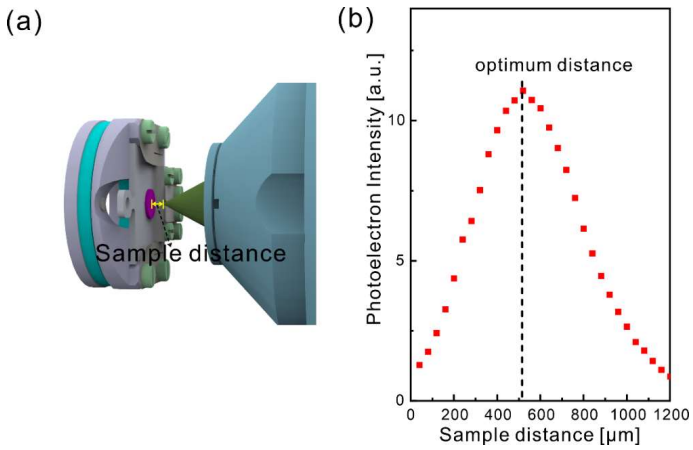

Supplementary Figure 5: XPS peak intensity with the sample distance. (a) The setup of the AP-XPS measurement; (b) The XPS peak intensity as a function of the sample distance.

The fluctuations in photoelectron intensity attributable to variations in sample distance can be corrected by normalizing against the background intensity. The bellow Supplementary Figure 6 presents the O 1s peak intensities for both the gas phase and PtO_x, calibrated relative to the background. This calibration reveals that the intensity of the gas peak remains consistent, whereas the intensity of the calibrated PtO_x peak escalates to its apex.

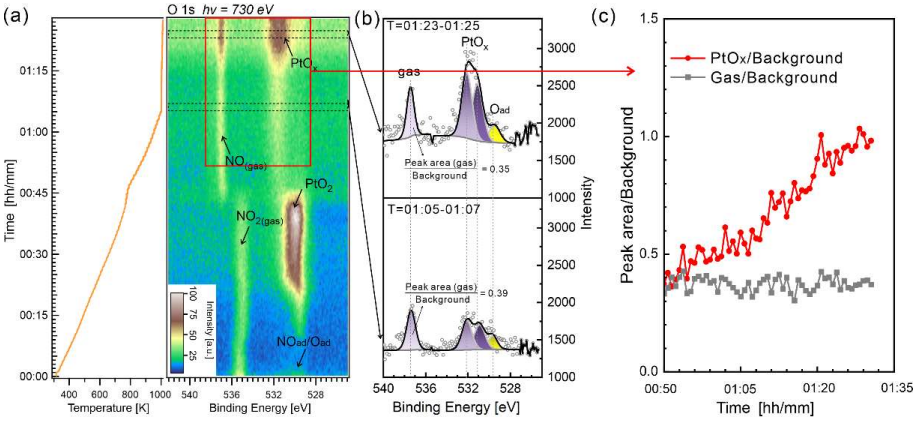

Supplementary Figure 6: Calibration of the XPS signal. (a) Evolution of the O 1s spectra during the oxidation process on Pt(111) surface under 1 mbar NO_2 from 300 to1000 K; (b) The O 1s spectra collected different time under 1000 K; (c) The ratio of the gas phase and the PtO_x to the background.

Supplementary Note 4: The depth profile experiment

The depth profile experiment was performed by collected the Pt 4f spectra under different photo energy. As shown in Fig. 1d of the main text, the Pt 4f spectra (Pt $4f_{5/2}$ = 71.9 eV) was obtained at 1000 K with the photon energy of 270 eV, 200 eV and 150 eV, respectively. The inelastic mean free paths (IMFP) of Pt 4f photoelectrons excited at these energies were approximately 4.6 Å, 4.0 Å, and 3.6 Å, respectively. As the X-ray detection depth decreased, the percentage of the oxide species increases. It indicated the oxide species formed on the very surface. Moreover, the O 1s

photoelectrons collected at 730 eV had the same IMFP as the Pt 4f photoelectrons excited at 270 eV.

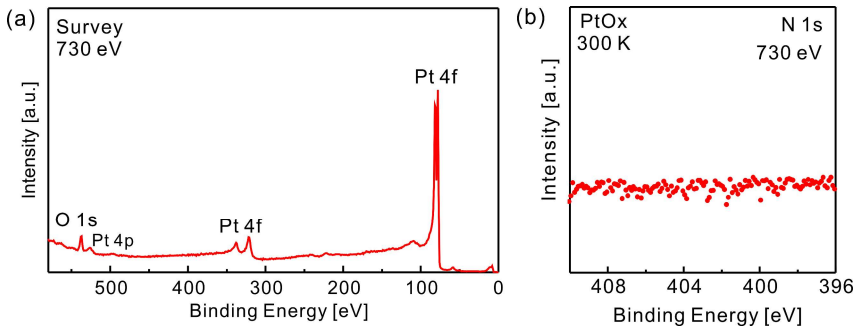

Supplementary Figure 7: Survey and N 1s spectrum. (a) Survey of the PtO_x under 1 mbar NO_2 at 1000 K; (b) N 1s spectrum on the PtO_x surface at 300 K. There were no other contaminations on the PtO_x surface.

Supplementary Note 5: The O/Pt atomic ratio calculation

The O/Pt atomic ratio was calculated from the peak area (S) of each species, ionization cross section (σ) of each element and photo flux under the incident photo energy. Using the following formula:

$$\frac{O}{Pt} = \frac{S_O}{S_{Pt}} \cdot \frac{\sigma_{Pt}}{\sigma_O} \cdot \frac{Flux_{@hv,Pt}}{Flux_{@hv,O}}$$

The photoionization total cross section and asymmetry parameters can be obtained from the database (https://vuo.elettra.eu/services/elements/WebElements.html). Specifically, the cross section for Pt 4f and O 1s are 3.286 (hν = 200 eV) and 0.3384 (hν = 660 eV), respectively. According to the above methods, the O/Pt ratio of the adsorbed species can be calculated to be ~2.7:1.

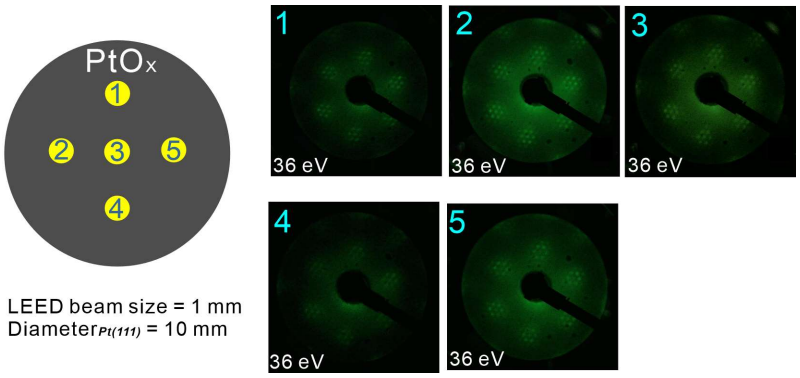

Supplementary Figure 8: LEED patterns of PtO_x covered Pt(111) surface at different positions.

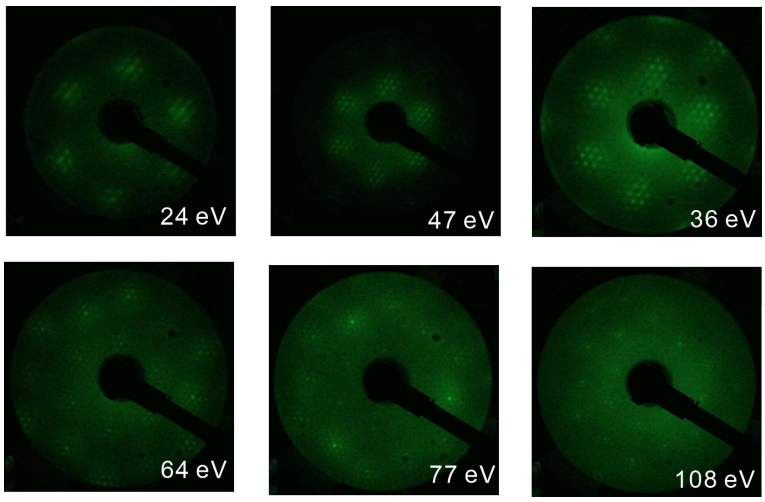

Supplementary Figure 9: LEED patterns at the same position under different energies.

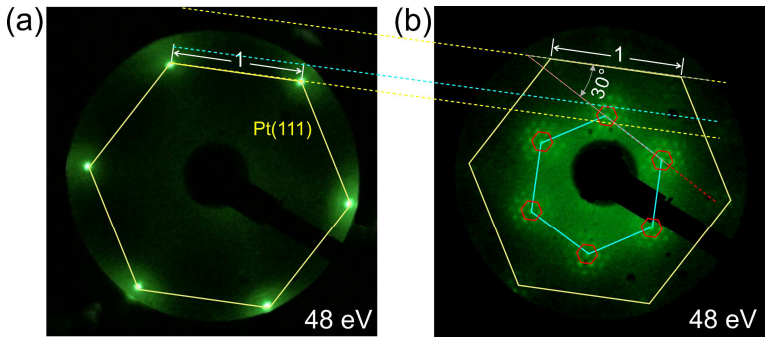

Supplementary Figure 10: Comparison of the LEED patterns. (a) LEED pattern of the clean Pt(111) surface; (b) LEED pattern of the PtO_x covered Pt(111) surface collected at the same direction with (a). It shows that the direction of the PtOx lattice is same with the Pt(111)'s direction, and the moiré superlattice is rotated 30° to the Pt(111) lattice.

Supplementary Note 6: Molecular dynamics (MD) simulations

In the MD simulations, the model's supercell consists of 288 O atoms present in both the PtO_x structure and the original α-PtO_2 structure. Further insights can be gained through Supplementary Figure 11 and 12, where spontaneous appearance of a moiré pattern is observed after structural relaxation (Supplementary Figure 12), with a lattice constant measured at 36.03 Å which is matched to LEED observation.

The strong bonds between lower-layer O and metallic Pt were explained by the analysis of the molecular orbital. Analysis of the molecular orbital has been utilized to understand the interaction between the 2pz orbital in the lower layer O of PtO_x and the 5dz2 orbital in the upper layer of metal Pt. The distribution of occupied molecular orbitals of the PtO_x/Pt is displayed in Fig. 3d3, revealing an orbital coupling between the 2pz orbital in the lower layer O of PtO_x and the 5dz2 orbital in the upper layer of metal Pt. Therefore, these simulations highlight that interface bonding interaction between Pt and O is crucial in ensuring thermodynamic stability (Fig. 3d3).

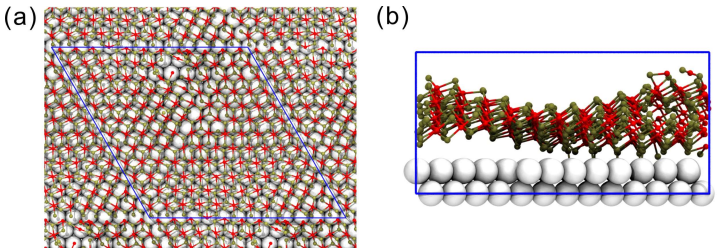

Supplementary Figure 11: The stability of 30° rotated α-PtO_2. (a) The atomic model of the α-PtO_2; (b) The sectional view of the relaxed α-PtO_2 structure. It floated on the Pt(111) surface, which means that this structure is unstable.

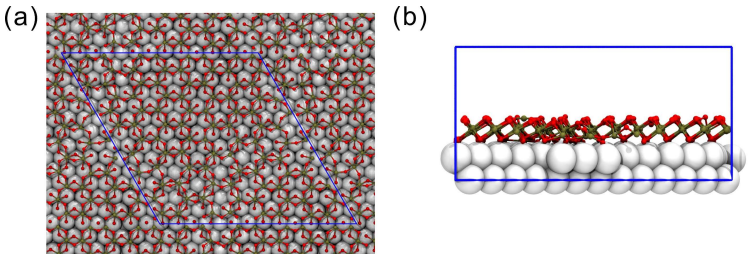

Supplementary Figure 12: The stability of PtO_x. (a) The atomic model of the relaxed PtOx on Pt(111) surface; (b) The sectional view of the relaxed PtO_x structure. It fit on the Pt(111) surface closely, which means that this structure is stable.

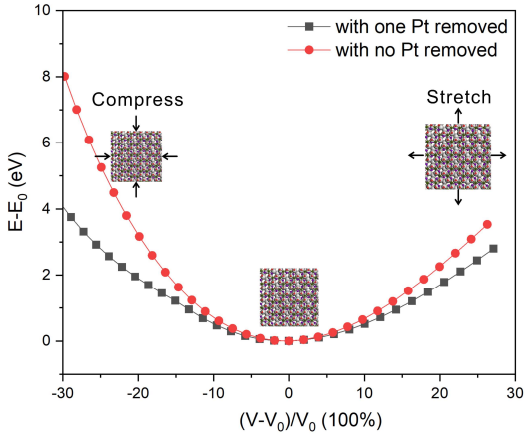

Supplementary Figure 13: Calculation of the energy as a function of volume of the PtO_x/Pt(111). Using the Murnaghan equation,[8] we could get the bulk modulus of PtO_x on Pt(111) is 0.011 eV/Å^3 with one Pt removed, 0.007 eV/Å^3 with no Pt removed.

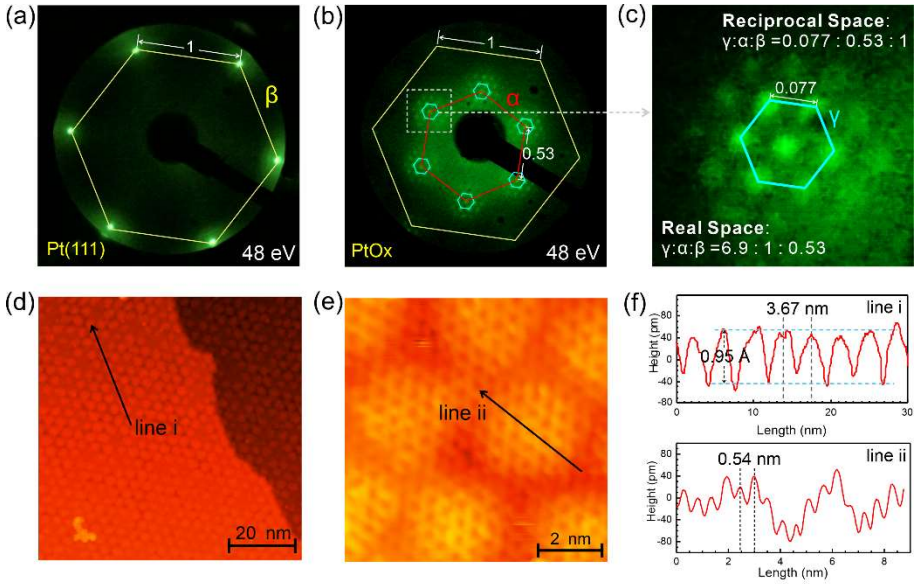

(g)

Length [nm]	STM	LEED
Metallic Pt lattice	0.28	0.28
Red moire pattern	0.54	0.53
Green moire pattern	3.67	3.65

Supplementary Figure 14: Characterization of the PtO_x thin film by STM and LEED. LEED patterns of the clean Pt(111) surface (a), the PtO_x thin film covered surface (b), (c) Enlarged image of region in green box in (b). STM images of large-scale (d) and high-resolution (e) STM images of PtO_x thin film covered surface; (f) the corresponding line profiles of the labeled line in (d) and (e), respevtively; (g) Comparison of the lattice constants obtained from the STM and LEED results. The LEED patterns were collected under the same energy follow the same direction. Tunneling parameters: (d) Vs=1.59 V, I= 0.07 nA; (e) Vs=0.89 V, I= 0.07 nA.

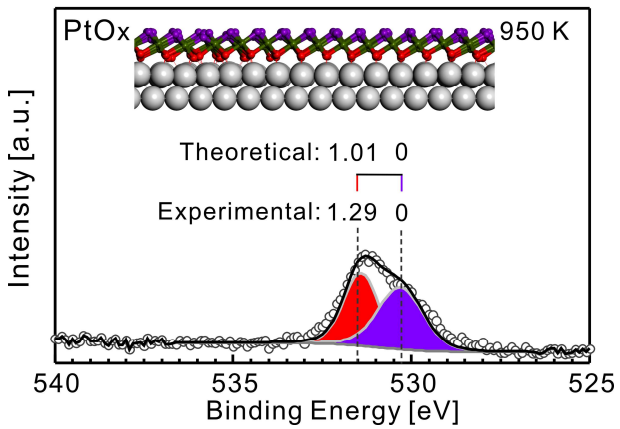

Supplementary Figure 15: O 1s spectrum of PtO_x. It shows the experimental and the calculated binding energy of the surface oxygen atom and interface oxygen atom.

Supplementary Note 7: The valence state and coordination of Pt atoms in PtO_3-Pt species

Before exploring the stability of the PtO_3-Pt structure, we delved into the coordination of Pt atoms, traditionally understood to be fully saturated in α-PtO_2 structures. Intriguingly, our investigation revealed a distinction between PtO_3-Pt and α-PtO_2, some Pt atoms removed from the lattice of PtO_2, making the coordination of oxygen changed. These 'dangling' oxygen atoms would form strong O-Pt bonds with the metallic Pt substrate. Therefore, the term of PtO_3-Pt was used to describe this oxide, instead of PtO_3. This structural differentiation is supported by our XPS results, which demonstrated that the Pt 4f binding energy (BE) for PtO_3(-Pt), α-PtO_2, and metallic Pt were measured at 72.0, 71.9, and 70.9 eV, respectively, with an uncertainty of approximately 0.2 eV. Notably, the BE shift of PtO_3(-Pt) relative to metallic Pt (1.1 eV) closely approximates that of α-PtO_2 (1.0 eV), indicating a similar valence state between these two Pt oxide configurations.

To advance our analysis, we also conducted Bader charge calculations for PtO_3-Pt and bulk α-PtO_2 systems. The net charge of each atom was determined by subtracting the calculated Bader charge from its valence electron number. The calculated results are shown in Supplementary Figure 16, which illustrate the net charges averaged across each layer of PtO_3-Pt. Comparative assessment of electron gains and losses within the bulk α-PtO_2 context, vis-à-vis the valence states, led us to deduce that the Pt in PtO_3-Pt, exhibiting a valence state marginally above +4 but definitively below +6, accrues an electron gain of 1.81 |e|, as opposed to the 1.60 |e| associated with +4 valence state Pt. This discernibly lower valence state of PtO_3-Pt can be attributed to the electron transfer between the basal layer oxygen and the uppermost metallic Pt layer, as highlighted by our charge transfer analysis presented in Supplementary Figure 16a, wherein a substantial charge transfer of 0.36 |e| was observed from the metallic Pt to the bottom layer oxygen. These results suggest that the two-dimensional PtO_3 oxide is not an isolated structure but must be associated with a metallic Pt substrate.

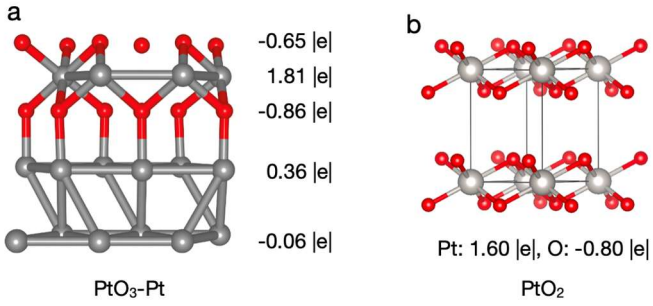

Supplementary Figure 16: Bader charges of PtO_3-Pt (a) and bulk α-PtO_2 (b). The net charges of PtO_3-Pt were averaged among each layer and labelled on the right.

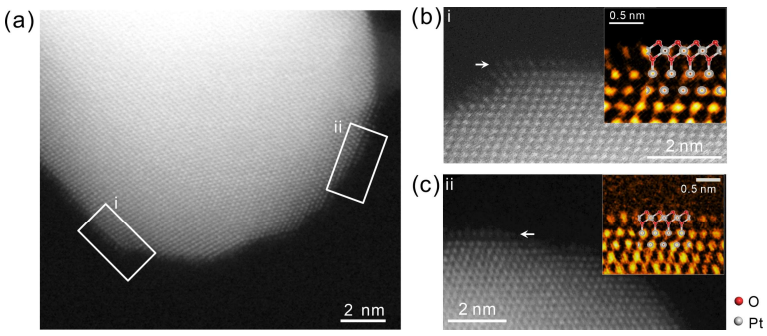

Supplementary Figure 17: STEM image of Pt nanoparticles under NO_2. (a) STEM image of Pt nanoparticles under NO_2 at 1000 K. (b) and (c) are the HAAD-STEM images in the labeled region i and ii in (a), respectively.

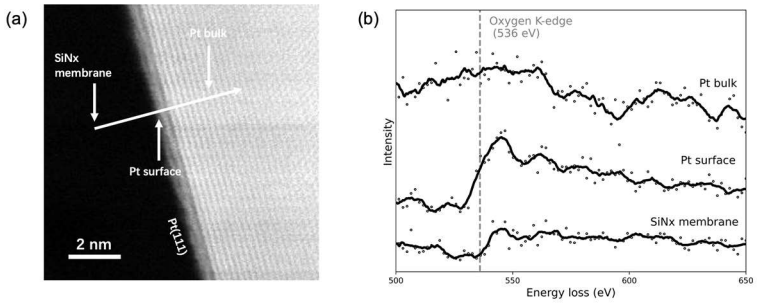

Supplementary Figure 18: EELS analysis of the surface species on Pt NPs. The annular dark filed (ADF) image (a) and electron energy loss spectroscopy (EELS) line-scan spectra (b). Oxygen K-edges were acquired along the marked arrow in the ADF image. A remarkable increase of oxygen signal was detected on the Pt(111) surface, indicating that the Pt(111) surface was oxidized by NO_2.

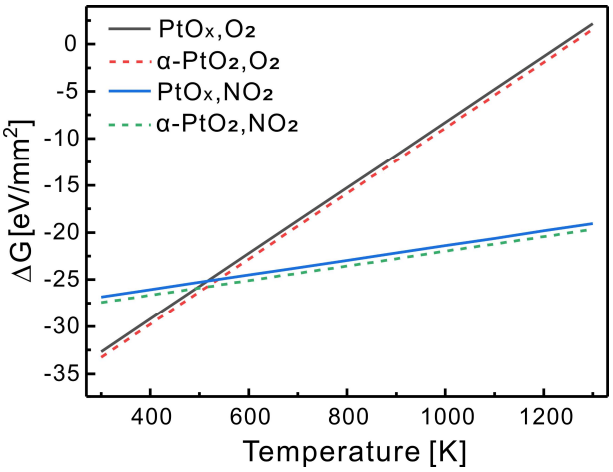

Supplementary Figure 19: The comparison of the free energy of the PtO_x (PtO_3-Pt) and α-PtO_2 under NO_2 or O_2 conditions.

Supplementary Note 8: The formation of PtO_3-Pt under O_2 conditions

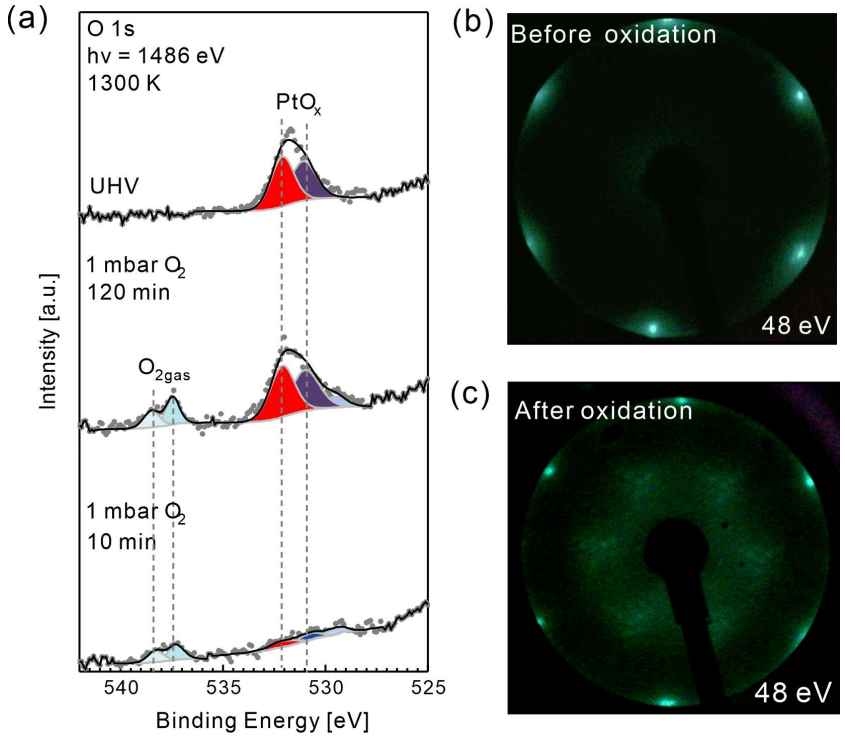

Supplementary Figure 20: Formation of PtO_x (PtO_3-Pt) on the Pt(111) surface under 1 mbar O_2 at 1300 K. (a) O 1s spectra on Pt(111) surface under different conditions at 1300 K; (b) and (c) LEED patterns on the Pt(111) surface at 48 eV collected before and after oxidation by O_2, respectively.

The formation of two-dimensional PtO_3-Pt (PtO_x) structures under O_2 conditions requires significantly elevated temperatures, as demonstrated in Supplementary Figure 20. Through observations at these higher temperatures in an O_2 atmosphere, we have demonstrated the emergence of PtO_3-Pt layers. These findings are substantiated by AP-XPS and LEED experiments, as shown in Supplementary Figure 20. Specifically, the O 1s spectra depicted in Supplementary Figure 20a confirm the presence of PtO_3-Pt on the surface across various conditions. Furthermore, the LEED patterns, detailed in Supplementary Figure 20c, indicate that the oxidized structure of the Pt(111) surface under O_2 conditions aligns with observations made under NO_2 conditions. This evidence collectively confirms the feasibility of forming two-dimensional PtO_3-Pt structures upon exposure to oxygen.

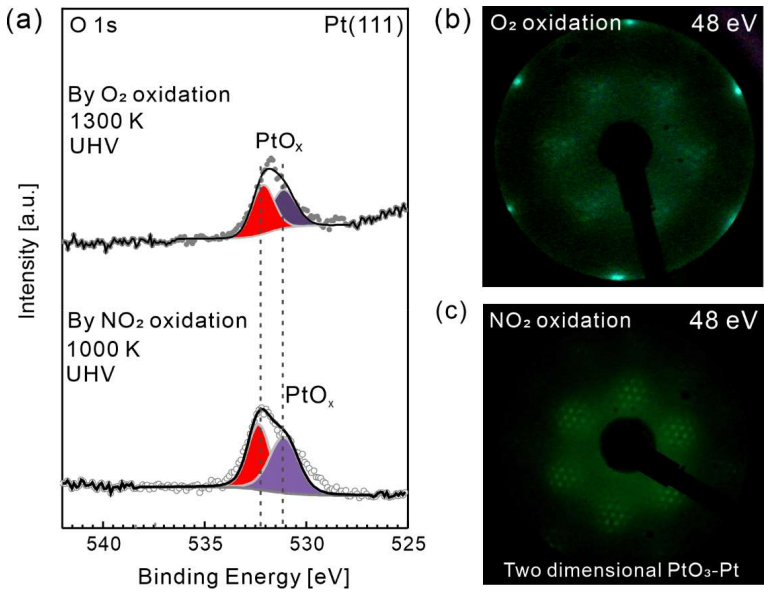

Supplementary Figure 21: Stability of PtO_x (PtO_3-Pt) on Pt(111) under O_2 and NO_2 conditions. (a) O 1s spectra of the PtO_x species formed under O_2 and NO_2 conditions, respectively; (b) and (c) LEED patterns of the PtO_x on Pt(111) under O_2 and NO_2 conditions, respectively.

Supplementary Note 9: The weaker affinity of α-PtO_2 for the Pt substrate than that of PtO_3-Pt

The transition from α-PtO_2 to PtO_3-Pt upon heating can be ascribed to the weaker affinity of α-PtO_2 for the Pt substrate than that of PtO_3-Pt. In the α-PtO_2 structure, the oxygen atoms are fully coordinated with the Pt atoms within the oxide layer, yielding adsorption energy on the Pt substrate of just -7.8 eV nm^{-2} obtained by DFT calculation. Conversely, the oxygen atoms in PtO_3-Pt lack full coordination and are inclined to establish additional Pt-O bonds with the metallic Pt atoms, leading to a significantly stronger adsorption energy of -22.4 eV nm^{-2}. Hence, when subjected to higher temperatures, the α-PtO_2 layers would evaporate or detach from the Pt substrate, revealing a reduced Pt surface.[9-11] The thermodynamic simulations offer a cogent explanation for the observed oxidation patterns of Pt and align well with experimental findings. Thermodynamic simulations provide a compelling rationale for the witnessed Pt oxidation trends and resonate with our experimental observations.

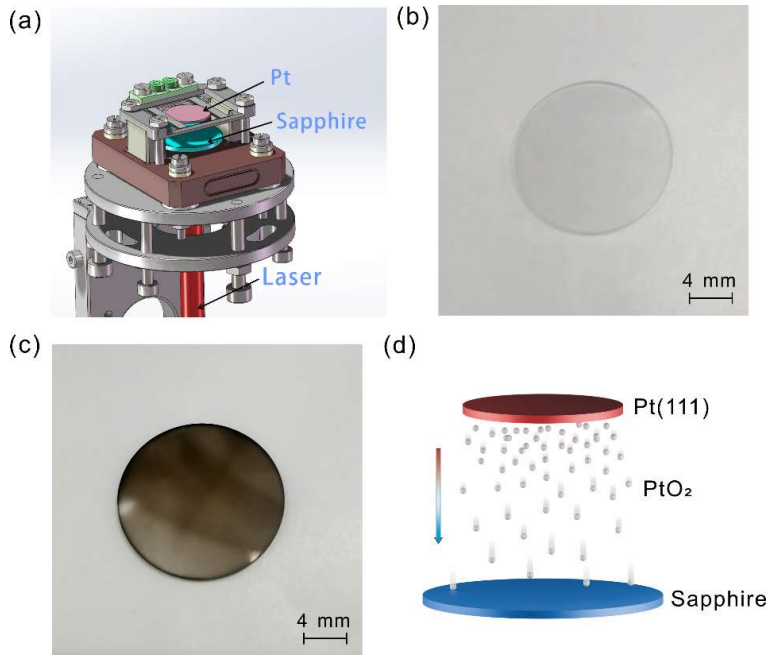

Supplementary Figure 22: PtO_2 evaporation under high temperatures. (a) The setup of the heating stage in an independent chamber. The Pt(111) was under 1 mbar NO_2 conditions from 300 K to 1000 K. And the sapphire window bellow the Pt(111) was to prevent the pollution. (b) and (c) the sapphire window before and after the Pt(111) oxidation, respectively, The PtO_2 evaporate from the Pt(111) surface at 750 K and blacked the sapphire window. (d) the diagrammatic figure of the PtO_2 evaporation.

Supplementary Note 10 Chemical reaction on PtO_3-Pt/Pt(111)

Previous studies have highlighted that the traditional forms of Pt oxide, surface oxide and PtO_2, exhibit distinctly different catalytic behaviors such as in CO oxidation and methane oxidation reactions.[3, 12-14] Given the unique surface electronic structure of the 2D crystallized PtO_3-Pt, we explored its catalytic capabilities in two benchmark reactions: CO oxidation and methane oxidation, as shown below.

The preparation of PtO_3/Pt(111) and the subsequent evaluation of its catalytic activity were carried out within a beamline AP-XPS analysis chamber, details of which are depicted in the Supplementary Figure 23. In this configuration, the reactant gases and photoelectrons travel concurrently through the nozzle. The gas composition is then analyzed by mass spectrometry at the location of the gas outlet part, as illustrated in the Supplementary Figure 23c, d. And, the sample was moved away to avoid the effect of nozzle on the surface reaction (Supplementary Figure 23e).

The mass spectrometer results of the chemical reaction of 0.1 mbar CH_4 + 0.1 mbar CO + 0.5 mbar CO on PtO_3/Pt(111) was shown in Supplementary Figure 23f. And the reaction on Pt(111) surface under the same conditions was used as a contrast. It is important to highlight that this setup results in a scenario where not all reactant gases are in contact with the Pt(111) surface. This limitation inherently affects the overall conversion efficiency, preventing the achievement of 100% conversion in CO oxidation, as shown in Supplementary Figure 23f, g.

The PtO_3/Pt(111) surface predominantly facilitated CO oxidation to CO_2 without significant

methane conversion. Conversely, the Pt(111) surface showed enhanced CO oxidation efficiency and also catalyzed methane oxidation at 800 K. This implies distinct selectivity in CO and methane oxidation reactions on PtO_3/Pt(111) compared to Pt(111). The details about the reaction on PtO_3/Pt(111) was shown as below.

For the nature of the catalyst post-reaction with CO and/or methane and the stability of the surface oxide, we have closely monitored the surface state of the two-dimensional PtO_3 during the catalytic reactions. The data captured in Supplementary Figure 24a demonstrates that the characteristic peak associated with PtO_3-Pt remains consistent, suggesting stability of the oxide layer throughout the catalytic process. Furthermore, the LEED patterns observed before and after the reactions, presented in Supplementary Figure 24b, c, confirm that the structural integrity of the oxide surface is largely preserved.

The reaction selectivity on PtO_3/Pt(111) surfaces is elucidated through mechanistic investigations. The selective oxidation of CO over CH_4 on PtO_3/Pt(111) is attributed to CO's adsorption ability on the PtO_3-Pt surface (Supplementary Figure 25), in contrast to CH_4's inertness under the same electronic states. The adsorbed CO can be oxidized by either lattice oxygen on PtO_3/Pt111 through the Mars–van Krevelen (MvK) mechanism or gaseous oxygen through the Eley-Rideal mechanism.[15-17] This behavior underscores the potential of 2D PtO_3-Pt films in specific chemical reactions and catalysis.

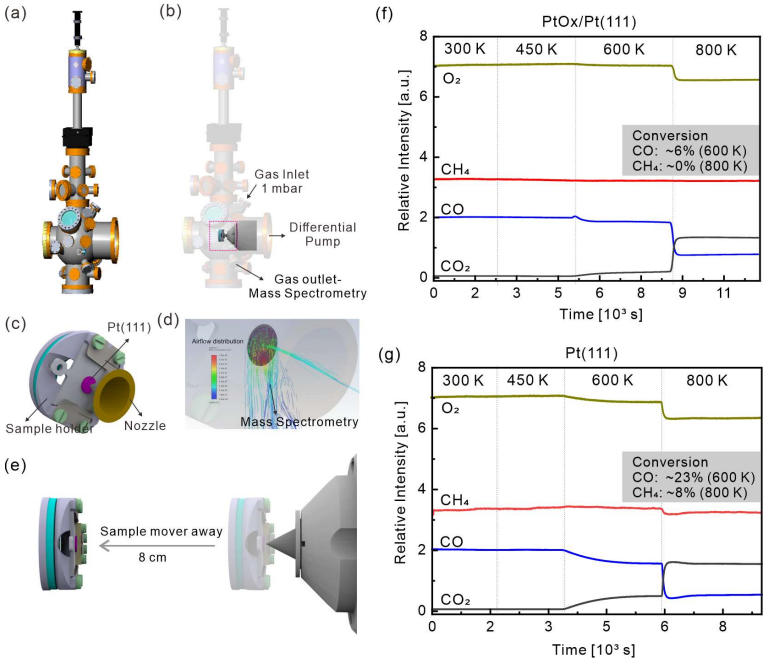

Supplementary Figure 23: The AP-XPS experimental setup and the mass spectrometer result of CH_4+CO+O_2 chemical reaction in the AP-XPS chamber. (a) and (b) The drawing of the AP-XPS's measurement chamber; (c) The enlargement of the red square in (b); (d) The simulation of the gas flow distribution above the sample under reaction conditions; (e) Sample move away during analyzing the gas component; (f) and (g) The mass spectrometer results of the chemical reaction of 0.1 mbar CH_4 + 0.1 mbar CO + 0.5 mbar CO on PtO_3/Pt(111) and Pt(111) surfaces, respectively.

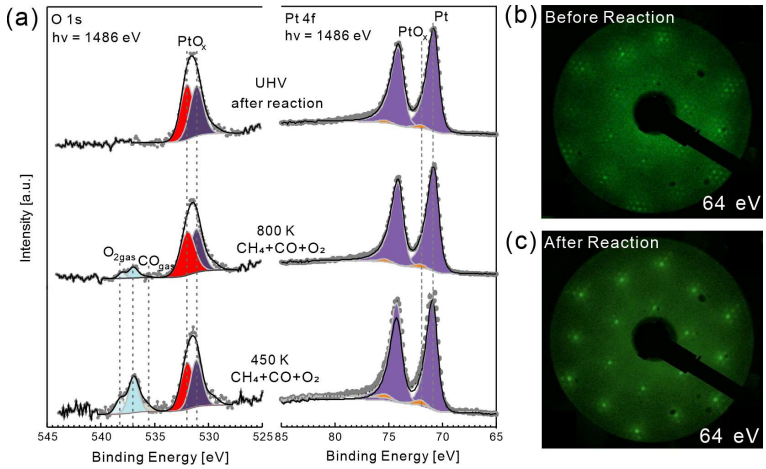

Supplementary Figure 24: XPS spectra and LEED patterns on PtO_3/Pt(111) during CH_4+CO+O_2 reaction. (a) (a) O 1s and Pt 4f spectra on PtO_3/Pt(111) during CH_4+CO+O_2 reaction; (b) LEED pattern of the as-prepared PtO_3-Pt/Pt(111); (c) LEED pattern on the PtO_3-Pt after the CH_4+CO+O_2 reaction.

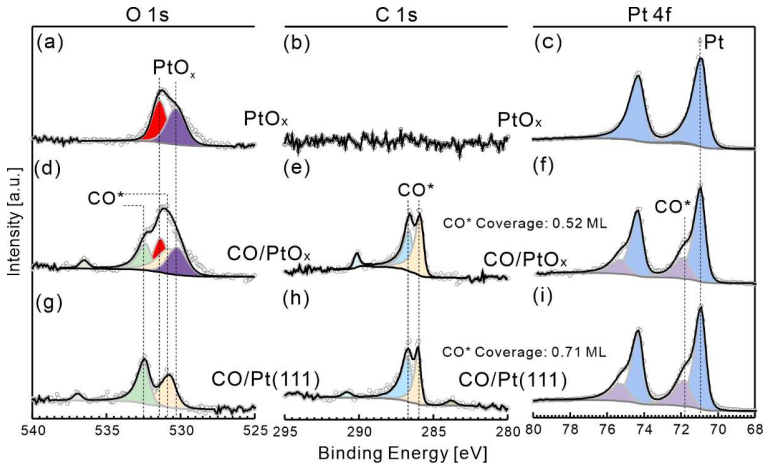

Supplementary Figure 25: XPS spectra of CO adsorption. The upper panel are the O 1s (a), C 1s (b) and Pt 4f (c) spectra of the as-prepared PtO_3/Pt(111), respectively; The middle panel are the O 1s (a), C 1s (b) and Pt 4f (c) spectra of CO adsorbed on the PtO_3/Pt(111) surface; The bottom panel are the O 1s (a), C 1s (b) and Pt 4f (c) spectra of CO adsorbed on the Pt(111) surface.

Reference

(1) Fantauzzi, Donato; Krick Calderón, Sandra; Mueller, Jonathan E; Grabau, Mathias; Papp, Christian; Steinrück, Hans-Peter; Senftle, Thomas P; Van Duin, Adri Ct; Jacob, Timo. Growth of Stable Surface Oxides on Pt(111) at Near-Ambient Pressures. *Angewandte Chemie International Edition* **2017**, *56* (10), 2594-2598.

(2) Van Spronsen, Matthijs A.; Frenken, Joost W. M.; Groot, Irene M. N. Observing the oxidation of platinum. *Nature Communications* **2017**, *8* (1), 429.

(3) Miller, Daniel; Sanchez Casalongue, Hernan; Bluhm, Hendrik; Ogasawara, Hirohito; Nilsson, Anders; Kaya, Sarp. Different reactivity of the various platinum oxides and chemisorbed oxygen in CO oxidation on Pt(111). *Journal of the American Chemical Society* **2014**, *136* (17), 6340-6347.

(4) Ellinger, C.; Stierle, A.; Robinson, I. K.; Nefedov, A.; Dosch, H. Atmospheric pressure oxidation of Pt(111). *Journal of Physics: Condensed Matter* **2008**, *20* (18), 184013.

(5) Miller, D. J.; Öberg, H.; Kaya, S.; Sanchez Casalongue, H.; Friebel, D.; Anniyev, T.; Ogasawara, H.; Bluhm, H.; Pettersson, L. G. M.; Nilsson, A. Oxidation of Pt(111) under Near-Ambient Conditions. *Physical Review Letters* **2011**, *107* (19), 195502.

(6) Krasnikov, S. A.; Murphy, S.; Berdunov, N.; Mccoy, A. P.; Radican, K.; Shvets, I. V. Self-limited growth of triangular PtO_2 nanoclusters on the Pt(111) surface. *Nanotechnology* **2010**, *21* (33), 335301.

(7) Hawkins, Jeffery M.; Weaver, Jason F.; Asthagiri, Aravind. Density functional theory study of the initial oxidation of the Pt(111) surface. *Physical Review B* **2009**, *79* (12), 125434.

(8) Murnaghan, F. D. The Compressibility of Media under Extreme Pressures. *Proceedings of the National Academy of Sciences* **1944**, *30* (9), 244-247.

(9) Plessow, Philipp N.; Abild-Pedersen, Frank. Sintering of Pt Nanoparticles via Volatile PtO_2: Simulation and Comparison with Experiments. *ACS Catalysis* **2016**, *6* (10), 7098-7108.

(10) Krier, C. A.; Jaffee, R. I. Oxidation of the platinum-group metals. *Journal of the Less Common Metals* **1963**, *5* (5), 411-431.

(11) Chaston, Jc. Reactions of oxygen with the platinum metals. *Platinum Metals Review* **1965**, *9* (2), 51-56.

(12) Tsuji, Yuta; Yoshizawa, Kazunari. Adsorption and Activation of Methane on the (110) Surface of Rutile-type Metal Dioxides. *The Journal of Physical Chemistry C* **2018**, *122* (27), 15359-15381.

(13) Kummer, J. T. Catalysts for automobile emission control. *Progress in Energy and Combustion Science* **1980**, *6* (2), 177-199.

(14) Butcher, Derek R; Grass, Michael E; Zeng, Zhenhua; Aksoy, Funda; Bluhm, Hendrik; Li, Wei-Xue; Mun, Bongjin S; Somorjai, Gabor A; Liu, Zhi. In situ oxidation study of Pt (110) and its interaction with CO. *Journal of the American Chemical Society* **2011**, *133* (50), 20319-20325.

(15) Mars, P.; Van Krevelen, D. W. Oxidations carried out by means of vanadium oxide catalysts. *Chemical Engineering Science* **1954**, *3*, 41-59.

(16) Kim, Hyun You; Henkelman, Graeme. CO Oxidation at the Interface between Doped CeO_2 and Supported Au Nanoclusters. *The Journal of Physical Chemistry Letters* **2012**, *3* (16), 2194-2199.

(17) Taleblou, Mina; Camellone, Matteo Farnesi; Fabris, Stefano; Piccinin, Simone. CO Oxidation over Platinum Nanoclusters: Unraveling the Role of the Cluster Size and the Supporting Surface. *The Journal of Physical Chemistry C* **2023**, *127* (43), 21132-21149.